Check for updates

Bright self-trapped exciton emission in alkali iodide nanocrystals *via* Sn(II)-doping†

Xuemeng Wang,[a] Zan Dou,[a] Cong Tao,[a] Gaoyu Chen,[a] Qi Wei,[b] Haoyu You,[c] Xiaowang Liu,[a] Yatao Zou,[a] Nannan Han[a] and Weidong Xu [ID] *[ad]

Lead-free alkali halides have gained increasing attention owing to their desired optoelectronic properties across a variety of light-emitting applications. However, state-of-the-art alkali halide emitters commonly are bulky crystals functionalized with highly toxic elemental doping, hindering their integration into emerging flexible, wearable and large-area optoelectronic devices. Herein, we have developed environmental friendly and solution-processable alkali halide nanocrystals that exhibit intense self-trapped emission facilitated by Sn^{2+} ionic doping. We find that the presence of Sn^{2+}-interstitial leads to the tilting of cubic structures of RbI and thus triggers the self-trapped emission. The resultant tin(II)-doped RbI and $Rb_xCs_{1-x}I$ nanocrystals display an impressive maximum photoluminescence quantum yield of 91.9% and exhibit remarkable stability under ambient conditions. These findings pave the way for a new class of bright, solution-processable alkali halides, with diverse applications such as energy down conversion and flexible scintillation technologies.

[a] *Frontiers Science Center for Flexible Electronics, Xi'an Institute of Flexible Electronics (IFE), Northwestern Polytechnical University, 127 West Youyi Road, Xi'an 710072, China. E-mail: ifewdxu@nwpu.edu.cn*

[b] *Department of Applied Physics, The Hong Kong Polytechnic University, Hung Hom, Kowloon, Hong Kong*

[c] *Shaanxi Provincial Key Laboratory of Papermaking Technology and Specialty Paper Development, College of Bioresource Chemical and Materials Engineering, Shaanxi University of Science & Technology, Xi'an 710021, P. R. China*

[d] *Henan Institute of Flexible Electronics (HIFE) and School of Flexible Electronics (SoFE), Henan University, 379 Mingli Road, Zhengzhou 450046, China*

† Electronic supplementary information (ESI) available. See DOI: https://doi.org/10.1039/d4tc01428f

Weidong Xu has been a professor in the Institute of Flexible Electronics at Northwestern Polytechnical University since 2022. He received his PhD degree in Materials Science from Nanjing University of Posts and Telecommunications, China in 2016. Later, he moved to Linköping University, Sweden as a postdoc researcher and conducted principal research engineering (2017–2022). His group currently focuses on research on halide perovskites and lead-free metal halides for optoelectronics devices.

Weidong Xu

1. Introduction

With the rising of metal halide perovskites in photovoltaics[1] and light-emitting diodes (LEDs),[2,3] lead-free metal halides have gained considerable attention due to their low toxicity and versatility in crystal structures, along with their varied optoelectronic properties. This study was focused on developing novel lead-free metal halides including lead-free perovskite ABX_3, (*e.g.* $CsSnX_3$ (X = Cl, Br, I)), $A_3B_2X_6$ (*e.g.* $Cs_3Bi_2I_9$), and double perovskites (*e.g.* $Cs_2AgInCl_6$).[4–6] These compounds show promise in a range of applications beyond solar cells and LEDs,[7] such as in X-ray[8–11] and gamma-ray imaging, biological sensing,[12] and as photodetectors.[13]

Among lead-free metal halides, alkali halides such as NaI, CsI and RbI are well-known emitters with proven effectiveness in radioluminescence.[14] In general, these materials are able to deliver bright emission and excellent light yields of around 40 000–50 000 ph per MeV.[15] However, it is notable that their outstanding photoluminescence or radioluminescence emissions at room temperature are triggered by doping with highly toxic elements such as CsI: Tl and NaI: Tl, which are two of the most widely used scintillators for radiation detection and imaging since 1948.[16] In addition, these materials were synthesized as bulky single crystals with high cost, making them hardly compatible with flexible and wearable applications. Considering their excellent emission properties and radioluminescence performance, it is highly promising to develop cost-effective and environmental friendly alkali halide emitters that are compatible with flexible and printing manufacturing techniques.

9978 | *J. Mater. Chem. C*, 2024, **12**, 9978–9985

This journal is © The Royal Society of Chemistry 2024

In this work, we achieved bright self-trapped exciton (STE) emission in rubidium iodide (RbI) nanocrystals at room temperature through Sn^{2+}-doping. Specifically, with a mere 1.8% Sn incorporation, the RbI nanocrystals demonstrated broad-band yellow emission with a high photoluminescence quantum yield (PLQY) of approximately 91.9%, among the best for metal halides with STE emission. Theoretical analysis indicates that Sn^{2+} cations act as interstitials, causing tilts in the RbI crystal structure that generate sub-bandgap states conducive to STE emission. Furthermore, we could modulate the emission from yellow to orange by alloying with Cs^+. Remarkably, our Sn^{2+}-doped nanocrystals remain stable under ambient conditions without the need for encapsulation, contrasting the sensitivity of Sn-based perovskites to oxygen and moisture.[17–19] Overall, our work not only unveils the first instance of alkali halide nanocrystals with bright emission at room temperature but also unlocks the potential of alkali halide emitters for a wide range of light-emitting applications such energy down conversion, flexible radioluminescence, and solar concentrators.

2. Experimental section

2.1 Chemicals

High-purity tin(II) iodide (SnI_2, 99.999%), rubidium acetate (Rb(OAc), 99.8%), and tri-n-octylphosphine (TOP, 90%) were sourced from Alfa. Cesium carbonate (Cs_2CO_3, 99%) and oleic acid (OA, 90%) were acquired from Sigma-Aldrich. Oleylammonium iodide (OAmI, 99.5%), 1-octadecene (ODE, 90%), oleylamine (OLA, 90%), and xylene (99.0%, SafeDry) were procured from Adamas and Aladdin. Dowtherm A (referred to as DA) and ethyl acetate (EtOAc, 99.8%) were supplied by Macklin and Innochem. TOP, OA, OLA, and DA were pre-treated at 120 °C under vacuum for two hours to remove any moisture. Other reagents were used as received without further purification.

2.2 Preparation process

Synthesis of rubidium oleate (Rb-OA) precursor. Rb(OAc) (0.3613 g, 2.5 mmol), 8 mL of DA and 2 mL of OA were combined in a three-neck flask. The mixture was stirred vigorously and degassed for 30 minutes at 100 °C, it was then heated to 120 °C under a nitrogen atmosphere until a clear, transparent solution was achieved, indicating the complete reaction of Rb(OAc) with OA. The Rb-OA precursor was then transferred to a glove box before use.

Synthesis of tin(II)-doped rubidium iodide nanocrystals (RbI NCs). In an N_2-filled glove box, a mixture of SnI_2 (0.3725 g, 1 mmol), TOP (1 mL), OLA (200 μL), and DA or ODE (30 mL) was heated at 90 °C for 3 hours until all the SnI_2 was fully dissolved. The reaction temperature was carefully tuned from 30 to 120 °C. 4 mL of Rb-OA was rapidly injected into the Sn precursor mixture and allowed to react for 5 seconds before being quenched in an ice bath. Tin doping ratios were controlled by the Sn:Rb feed ratio, with OAmI providing an additional source of iodine.

Synthesis of tin(II)-doped rubidium-cesium iodide alloy nanocrystals ($Rb_xCs_{1-x}I$ NCs). Cs^+-alloyed NCs were prepared by following the tin(II)-doped RbI NC synthesis procedure, with the modification of substituting a specific molar fraction of Cs_2CO_3 for Rb(OAc). The resulting Sn^{2+}-doped RbI NCs and $Rb_xCs_{1-x}I$ RbI NCs crude solutions were mixed with an antisolvent, EtOAc (1:1 v/v), and precipitated by centrifugation at 14 000 rpm for 5 minutes. The resulting precipitate was collected and redispersed in xylene to create a colloidal dispersion of the NCs.

2.3 Characterization

Optical measurements. A MAPADA UV-670 spectrometer was used to obtain the absorption spectra. The temperature-dependent photoluminescence spectra were measured using the Ocean Insight QE pro spectrometer with a laser excitation (350 nm) at different temperatures in a closed-circuit liquid nitrogen system. Time-resolved PL spectra were collected using an Optoscope-SC streak camera system, which has an ultimate temporal resolution of ∼10 ps. The laser source was a Coherent Legend regenerative amplifier (150 fs, 1 kHz, 800 nm) seeded by a Coherent Vitesse oscillator (100 fs, 80 MHz). The emission from the samples was collected at a backscattering geometry using a pair of lenses and into an optical fiber that was coupled to a spectrometer (Acton, Spectra Pro 2500i) to be detected by a charge-coupled device (Princeton Instruments, Pixis 400B).

Structural analysis. X-ray diffractometer (XRD) patterns of the samples were obtained using a Bruker D8 Advance using a Cu-Kα target. Transmission electron microscopy (TEM) images were obtained using a HITACHI HT7800 microscope operated at 100 kV. The high-resolution transmission electron microscopy (HRTEM) and energy dispersive X-ray spectroscopy (EDS) were carried out using a JED 2300T TEM. X-ray photoelectron spectroscopy (XPS) measurements were performed on a Kratos AXIS Ultra DLD spectrometer.

Density functional theory (DFT) calculations. All calculations were performed using the Vienna ab initio simulation package based on the density functional theory.[20–25] Perdew–Burke–Ernzerhof (PBE) functional under generalized gradient approximation was applied to describe the exchange–correlation interaction between electrons, and the interaction between electrons[26] and atoms is described by the projector augmented plane-wave method. The energy cutoff was set to 500 eV. The convergence criteria for energy and force were 10^{-5} eV and 0.01 eV Å^{-1}, respectively. We optimized the structure and performed electronic property calculations by using the $3 \times 3 \times 3$ k-mesh.

3. Results and discussion

The synthetic protocols are shown in Fig. 1a. In brief, the Sn^{2+}-doped RbI NCs were achieved by employing a classic hot injection method in an N_2-filled glove box, where rubidium oleate (Rb-OA) precursor was quickly injected into SnI_2/tri-n-octylphosphine (TOP) precursors. For reference purposes, we also prepared RbI NCs without the incorporation of Sn^{2+} cations, and the TEM image is shown in Fig. S1 (ESI†). We first
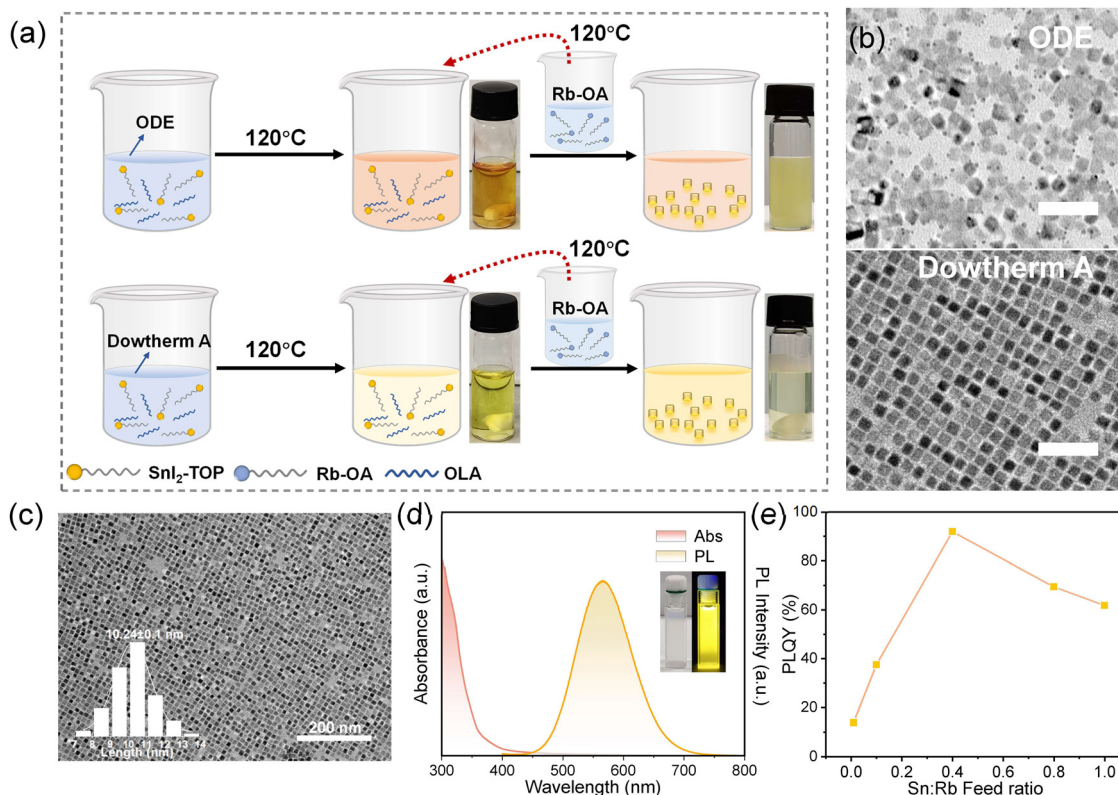
Fig. 1 (a) Synthetic procedures of Sn^{2+}-doped RbI NCs by a hot injection method in a glove box, highlighting the critical role of different solvents (ODE and DA) in determining the quality of NCs. (b) TEM images of the NCs prepared with ODE (up panel) and DA (bottom panel) as the solvent (scale bar, 50 nm). (c) TEM image of optimized Sn^{2+}-doped RbI NCs showing size distribution. (d) Absorbance and PL spectra of Sn^{2+}-doped RbI NCs. (e) The dependence of PLQYs on the Sn : Rb feed ratio.

started with 1-octadecene (ODE) as the solvent but realized that this commonly used solvent for synthesizing colloidal nanocrystals is not a good choice for those NCs with Sn^{2+}. Our observations indicated that at high temperatures (≥ 120 °C), the SnI_2–TOP solution in ODE transitions from yellow to brown, which is a typical sign of polyiodide formation because of the redox reaction during the synthesis of Sn^{2+}-based nanocrystals.[27] It consequently leads to uneven size distribution of NCs and the formation of a large number of crystal defects (Fig. 1b, upper panel), which usually are detrimental to the emission characteristics.

To mitigate the formation of polyiodides, we utilized an aromatic mixture, Dowtherm A (referred to as DA, composed of 26.5% diphenyl and 73.5% diphenyl oxide) instead of the conventionally used ODE as the solvent,[27] which is well-known for the excellent chemical stability. In addition, the electron-donating property of diphenyl oxide could be helpful for impeding the oxidation of Sn^{2+}. The resulting nanocrystals exhibited a typical cubic shape with uniform size distribution (Fig. 1b, down panel). Further calculation yielded an average size of approximately ~ 10 nm, as presented in Fig. 1c. Notably, a high injection temperature is key to realizing monodispersed size distribution, and the optimized temperature is 120 °C (Fig. S2, ESI†). In Fig. 1d, UV-vis absorption and PL emission spectra of Sn^{2+}-doped RbI NCs are displayed. The PL spectrum features a broad-band emission peaking at 568 nm with a large

full-width at half-maximum (FWHM) of 105.7 nm. The PL excitation (PLE) spectrum is displayed in Fig. S3 (ESI†), from which a serious of excitonic features are observed. The Stokes shift is ~ 204 nm, as determined by the PLE peak with the lowest energy and PL emission. We note that the use of different solvents has no effect on the absorption and emission peaks but changes the photoluminescence quantum yield (PLQY) significantly (Fig. S4, ESI†). Fig. 1e illustrates the dependence of PLQYs of NCs as a function of the Sn^{2+} : Rb^+ feed ratio during synthesis. The highest PLQY, 91.9%, was achieved with a 40% molar ratio of Sn^{2+} relative to Rb^+. This result contrasts sharply with that of the Sn^{2+}-doped RbI NCs synthesized by ODE (24.3%). Besides, the over-addition of Sn^{2+} gives rise to a decrease in PLQYs, possibly due to the severe lattice distortion triggered by impurity doping.[28,29] Notably, akin to RbI single crystals that do not emit at room temperature,[30] this non-emissive property is also observed in their corresponding nanocrystals, suggesting the critical role of Sn^{2+} addition on triggering the emission properties.

To understand the mechanisms behind the PL emission of RbI NCs triggered by Sn^{2+} addition various structural characterizations were performed. Fig. 2a displays the morphological image of high-resolution transmission electron microscopy (HRTEM), where the presence of clear lattice fringes in the Sn^{2+}-doped RbI NCs underscores their high crystallinity. The interplanar distance
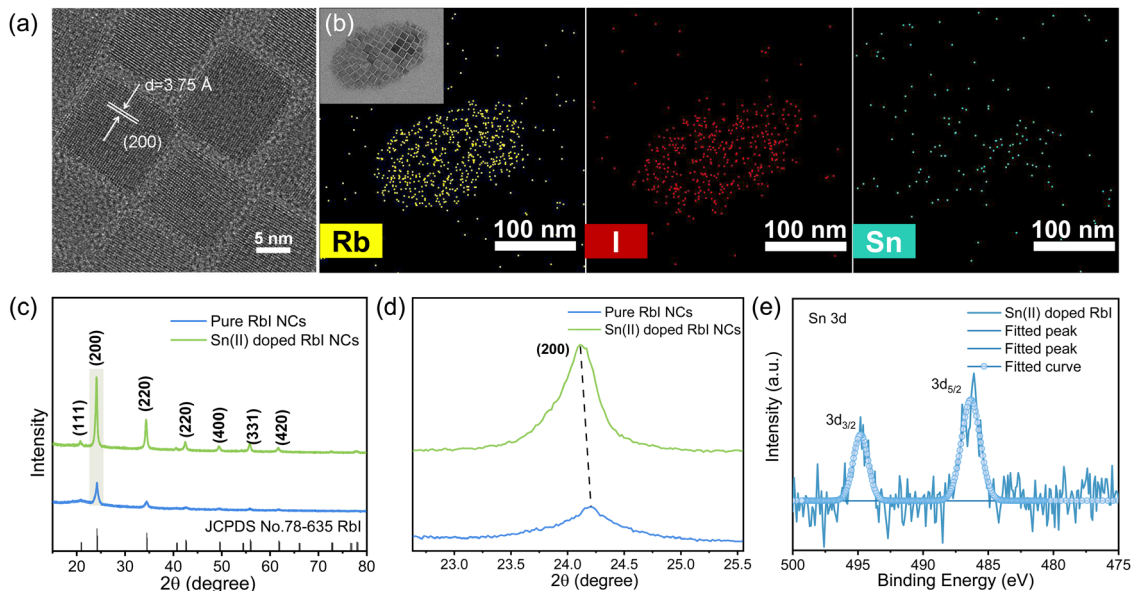
Fig. 2 (a) A HRTEM image of the Sn^{2+}-doped RbI NCs. (b) Elemental mapping for Rb, I and Sn, along with the relevant HAADF morphological image. (c) XRD patterns for RbI NCs and those with Sn^{2+} doping. (d) A focused comparison of the (200) crystal plane as extracted from the XRD patterns in Fig. 2c. (e) XPS core-level spectra of Sn 3d.

is 3.75 Å, slightly larger than the (200) plane of the cubic phase of RbI is 3.66 Å (Fig. 2a). Such an observation suggests lattice expansion as a result of Sn^{2+} doping.[31] We show energy-dispersive spectroscopy (EDS) elemental mapping in Fig. 2b, from which homogeneous distributions of Rb^+ and I^- ions across the crystal matrix are clearly visible. Notably, despite substantial incorporation of SnI_2 during the synthesis process (Rb : Sn molar ratio of 1 : 1), our EDS quantification reveals that only a small fraction of Sn^{2+} cations were retained, accounting for 1.86% of the total atomic composition (Fig. S5, ESI†).

Having confirmed the presence of Sn^{2+} in RbI NCs, we next performed X-ray diffraction (XRD) for the NCs thin films, aiming to determine whether the Sn^{2+} is incorporated within the crystal lattice or adsorbed on the crystal surface. Fig. 2c shows a comparison of the XRD pattern between pure RbI NCs and that after Sn^{2+} addition. We also show the standard JCPDS #78-635 card for reference. For both kinds of nanocrystals, the diffraction peaks well agreed with those from the references, suggestive of little changes in the crystal structures despite Sn addition. We also note that the doped samples show higher diffraction intensity and thus indicate a better crystallinity.[32] Importantly, the XRD patterns for Sn-doped samples slightly shifted to lower two theta with respect to the reference samples as shown in Fig. 2d, suggesting an expansion of the crystal lattice.[33] These results are in line with the HRTEM results, collectively confirming that Sn^{2+} ions are involved in the crystal lattice.

One consensus is that the divalent Sn ions are readily oxidized to quadrivalent once exposed to air, it is important to probe the valence of Sn cations and their chemical environment in the NCs. We thus performed X-ray photoelectron spectroscopy (XPS) for the doped and undoped samples. We show the XPS survey spectra in Fig. S6a (ESI†), and the core-level spectra of Sn

3d, Rb 3d and I 3d in Fig. 2e and Fig. S7 (ESI†). From Fig. 2e we see no evidence of Sn^{4+} formation, which is strikingly different from that in Sn^{2+}-based perovskites. We also observed a downward shift in the binding energies of Rb $3d_{3/2}$ and $3d_{5/2}$ peaks by approximately 0.54 eV, and I $3d_{3/2}$ and I $3d_{5/2}$ peaks by approximately 0.13 eV. Such shifts suggest changes in the chemical environment and the redistribution of their electron cloud of Rb^+ and I^- upon Sn^{2+} incorporation. Considering the variations in the binding energy of Rb 3d and I 3d, we speculate that the enhanced difficulties in the formation of Sn^{4+} could be assigned to the redistribution of electron density due to charge transfer that stabilized Sn^{2+}.

Having confirmed the incorporation of Sn^{2+} in the crystal lattice of RbI, we next performed a series of optical measurements to understand the photophysical behaviors of doped NCs. We realize that the large Stokes shift as well as the broad and symmetrical PL band are possibly the signs of emission from self-trapped excitons (STEs).[34,35] To further investigate whether the bright emission comes from STEs or defect-mediated emission,[36,37] we measured PL decay kinetics by time-correlated single-photon counting (TCSPC) technology. We show the PL decay curve in Fig. 3a, from which a double-exponential decay characteristic with a rapid yet minor decay component (~200 ns, 6.2%) can be observed. The fast component can be attributed to charge trapping. The average lifetime is as long as ~1050 ns, making it more likely to be STE emission. In addition, excitonic emission, such as STE emission, typically depends linearly on the excitation fluence,[38] but the defects-mediated emission displays sublinear behavior due to the limited number of trap states. We thus conducted the fluence-dependent PL measurements. We show the integrated PL intensity as a function of excitation fluence (from 0.016 to 11.742 mW cm^{-2}) in Fig. 3b, which clearly suggests a linear
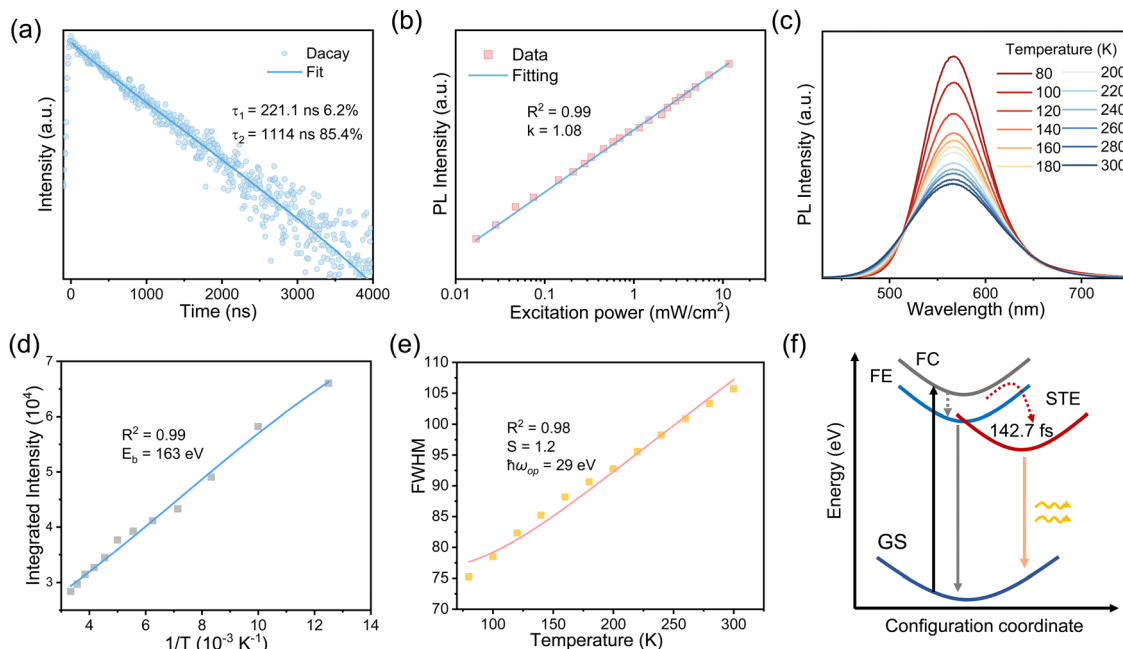
Fig. 3 The optical characterization of Sn^{2+}-doped RbI NCs. (a) TRPL decay curve. (b) Integrated PL emission intensity as a function of excitation power density. (c) Temperature-dependent PL spectra (80–300 K). (d) and (e) Integrated PL emission intensity (d) and FWHM (e) as a function of the temperature extracted from Fig. 3c. (f) The energy diagram depicting the STE processes. Here GS, FE, and FC refer to ground states and the states for free excitons and free carriers, respectively.

dependence. All these results indicate that the bright emission of Sn^{2+}-doped RbI stems from STEs.

In this regard, we proceeded to measure the temperature-dependent PL (80–300 K). As shown in Fig. 3c, the PL intensity increases with decreasing temperatures, owing much to the decreases in electron–phonon coupling or thermal-enhanced charge trapping.[39] Fig. 3d depicts the integrated PL intensity as a function of temperatures, where exciton binding energy was calculated by fitting the Arrhenius equation:[40,41]

$$I(T) = \frac{I_0}{1 + Ae^{(-E_b/k_BT)}} \quad (1)$$

where $I(T)$ is the PL intensity at temperature T, I_0 is the PL intensity at 0 K. E_b is the exciton binding energy. A is the fitting constant and k_B is the Boltzmann constant. The fitted results suggest a large E_b value of ~163 meV, suggesting that the electron–hole pair is a typical Frenkel exciton. As such, the PL emission is generated by the bound excitons instead of the free charge carriers, in line with the above conclusions that the emissions are from the recombination of STEs.

Furthermore, we investigated the PL line broadening as a function of temperature to understand the electron–phonon coupling, which is closely related to the full width at half maximum (FWHM) of the emission bands. The broadening was analyzed using the following relation:[42]

$$\text{FWHM} = 2.36\sqrt{S}\hbar\omega_{\text{phonon}}\sqrt{\coth\frac{\hbar\omega_{\text{phonon}}}{2k_BT}} \quad (2)$$

where $\hbar$ is the reduced Planck constant, ω_{phonon} is the phonon

frequency, T is the temperature, and S represents the Huang–Rhys factor. In general, S can be calculated by fitting the temperature-dependent FWHM. As presented in Fig. 3e, the FWHM values increase with temperature, attributable to the interaction between excitons and phonons. The fitted S value is ~1.2 with the degree of fitting of 0.99 (R-squared), indicative of a moderate but strong enough electron–phonon coupling for STE emission. The optical phonon energy ($\hbar\omega_{\text{op}}$) is estimated to be ~29 meV. As such, the time for the free excitons (FE) to be trapped into STEs ($\tau = 2\pi/\omega_{\text{phonon}}$) can be calculated as 142.7 fs, suggestive of an ultrafast transition from FE to STE states. The observed FWHM broadening with rising temperature and thus the distinct Fröhlich interaction with optical phonons are widely visible in polar semiconductors,[43] which consistently demonstrated that the bright emission is a consequence of the formation of STEs due to Sn^{2+} incorporation.

To thoroughly understand the origin of STE emission, we conducted density functional theory (DFT) calculations to explore the potential sub-bandgap states arising from the addition of Sn^{2+} ions. We started from the model of pristine RbI cells (2 × 2 × 2) comprising 64 atoms. Accordingly, we introduced a Sn atom into the unit cell, placing it between the Rb and I atoms as an interstitial impurity. The resulting Sn–I interatomic distance was approximately 3.20 Å. The introduction of the interstitial Sn^{2+} leads to the expansion of the unit cells from 14.98 Å to 15.10 Å, as a result of its large ionic radius and the enhanced lattice distortion. The band structures, computed using the PBE exchange–correlation functional, are depicted in Fig. S8 and S9 (ESI†). For the pristine RbI, a direct bandgap of 3.77 eV is observed (Fig. S9, ESI†). In comparison, the
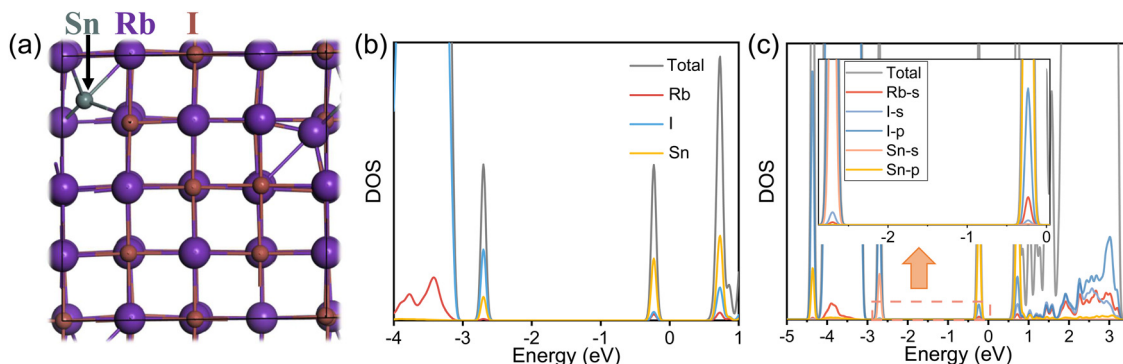
9982 | *J. Mater. Chem. C*, 2024, **12**, 9978–9985

This journal is © The Royal Society of Chemistry 2024

Fig. 4 (a) Supercell of cubic RbI with an interstitial Sn atom. (b) Total and partial DOS Sn–doped RbI calculated by the PBE method. (c) Orbital-projected DOS for Sn^{2+}-doped RbI calculated by the PBE method. The inset features an expanded view to highlight the sub-bandgap states.

introduction of Sn interstitials gives rise to three discernible sub-bandgap states, two of which are deep-lying states and indicate possible effects on optical transitions (Fig. S9c, ESI†), in line with the appearance of PLE bands. The density of states (DOS) diagrams in Fig. 4b show that Sn contributes to all the generated sub-bandgap states, especially those near the conduction bands. Further analysis of orbital-projected DOS suggests the critical role of Sn 5p orbitals in creating sub-bandgap states. All in all, we deduce that the Sn atomic orbitals hybridize with the crystal states of the host lattice, leading to sub-bandgap states corresponding to STE emission.

To assess the air stability of Sn^{2+}-doped RbI NCs, we measured their PLQYs over time under ambient conditions, with a humidity of approximately 35–55%. Fig. 5a shows that the PLQY of the NC thin films retains over 80% of its initial value after 10 hours of air exposure. Moreover, even after three weeks in the air, the thin films were still emissive. These findings suggest that our Sn^{2+}-doped RbI NCs are more resistant to oxygen and moisture than Sn-based perovskites, as detailed in Table S1 (ESI†). This much-enhanced stability may be attributed to the low Sn^{2+} content and/or the influence of the local electric structure, which could give rise to the different oxidation potential of Sn^{2+}. Overall, combined with their good stability, the excellent optical properties of these materials,

such as their bright emission with high quantum yields and large Stokes shifts, make them ideal for energy down-conversion applications, such as solar concentrators for silicon solar cells.[44] Additionally, their potential for radiation detection and imaging is promising, considering the inclusion of heavy metal cations and the widespread use of CsI: Tl.[14]

We also synthesized Rb^+/Cs^+ alloyed NCs by doping with Sn^{2+}, aiming to both demonstrate the versatility of our method and adjust the emission wavelengths. As shown in Fig. 5b, the PL spectra exhibited a red shift from 560 nm to 575 nm with the Cs^+ ratio increasing from 0% to 40%, resulting in a color change from yellow to orange. Such a shift can be assigned to the larger ionic radius of Cs^+ compared to that of Rb^+, which leads to the lattice expansion once Cs^+ is incorporated into the crystal structure. This speculation is supported by the XRD patterns shown in Fig. S10 (ESI†), which show a shift towards lower angles with higher Cs^+ concentrations. However, further increasing the Cs^+ content does not significantly affect the PL emission (Fig. S11, ESI†) or alter the XRD patterns. In addition, we found that it is very challenging to synthesize Sn^{2+}-doped CsI nanocrystals. Since $CsSnI_3$ conforms to Goldschmidt's rule for perovskite formation,[4,45] we speculate that there are competitive reactions toward the formation of $CsSnI_3$ and of Sn^{2+}-doped CsI during synthesis. This could result in non-uniform
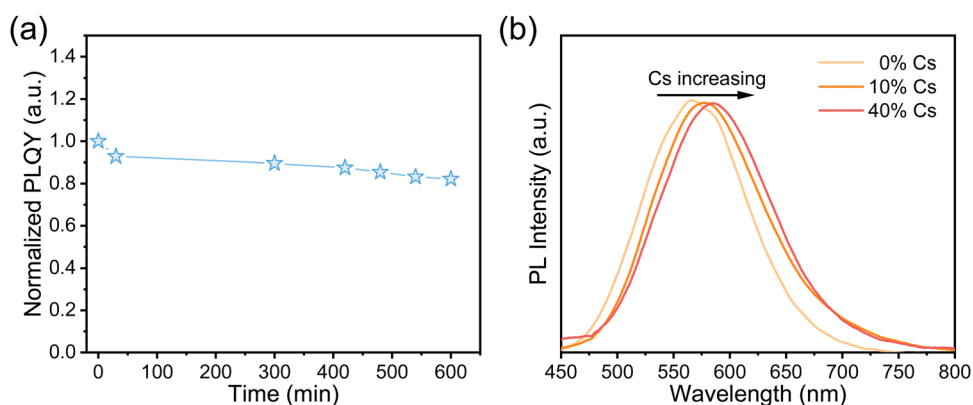

Fig. 5 (a) PLQYs of Sn^{2+}-doped RbI NCs over time under ambient conditions. (b) PL spectra of Sn^{2+}-doped $Rb_xCs_{1-x}I$ NCs with different content of Cs^+ during synthesis.

This journal is © The Royal Society of Chemistry 2024

J. Mater. Chem. C, 2024, **12**, 9978–9985 | **9983**

nucleation and crystallization. Consistently, we observe notable variations in size and an irregular shape of $Rb_xCs_{1-x}I$ nanocrystals (Fig. S12, ESI†), as well as decreased PLQYs with enhancement of Cs^+ content (Table S2, ESI†).

4. Conclusion

In summary, we have achieved strong and broadband emission in RbI nanocrystals *via* Sn^{2+} doping, delivering an impressive photoluminescence quantum yield of 91.9%. Such a bright yellow-light emission is attributed to the formation of self-trapped excitons, which arise from the incorporation of Sn^{2+} cations into RbI crystal lattices as interstitials and relevant generation of the sub-bandgap states. Furthermore, we have shown the capability to adjust the emission color by alloying with other alkali cations. Importantly, these Sn^{2+}-doped lead-free metal halide nanocrystals demonstrate remarkable shelf stability in air, in stark contrast to the air-sensitivity of the Sn-based perovskites, thereby paving the way for their potential applications in various light-emitting technologies.

Conflicts of interest

The authors declare no conflict of interest.

Acknowledgements

References

1 P. V. Kamat, J. Bisquert and J. Buriak, *ACS Energy Lett.*, 2017, **2**, 904–905.

2 W. Xu, Q. Hu, S. Bai, C. Bao, Y. Miao, Z. Yuan, T. Borzda, A. J. Barker, E. Tyukalova, Z. Hu, M. Kawecki, H. Wang, Z. Yan, X. Liu, X. Shi, K. Uvdal, M. Fahlman, W. Zhang, M. Duchamp, J.-M. Liu, A. Petrozza, J. Wang, L.-M. Liu, W. Huang and F. Gao, *Nat. Photonics*, 2019, **13**, 418–424.

3 M. Karlsson, Z. Yi, S. Reichert, X. Luo, W. Lin, Z. Zhang, C. Bao, R. Zhang, S. Bai, G. Zheng, P. Teng, L. Duan, Y. Lu, K. Zheng, T. Pullerits, C. Deibel, W. Xu, R. Friend and F. Gao, *Nat. Commun.*, 2021, **12**, 361–371.

4 Q. Liu, J. Yin, B.-B. Zhang, J.-K. Chen, Y. Zhou, L.-M. Zhang, L.-M. Wang, Q. Zhao, J. Hou, J. Shu, B. Song, N. Shirahata, O. M. Bakr, O. F. Mohammed and H.-T. Sun, *J. Am. Chem. Soc.*, 2021, **143**, 5470–5480.

5 Y. Zhang, Y. Liu, Z. Xu, H. Ye, Z. Yang, J. You, M. Liu, Y. He, M. G. Kanatzidis and S. Liu, *Nat. Commun.*, 2020, **11**, 2304–2315.

6 Y. Liu, A. Nag, L. Manna and Z. Xia, *Angew. Chem., Int. Ed.*, 2021, **60**, 11592–11603.

7 Y. Zou, P. Teng, W. Xu, G. Zheng, W. Lin, J. Yin, L. Kobera, S. Abbrent, X. Li, J. A. Steele, E. Solano, M. B. J. Roeffaers, J. Li, L. Cai, C. Kuang, I. G. Scheblykin, J. Brus, K. Zheng, Y. Yang, O. F. Mohammed, O. M. Bakr, T. Pullerits, S. Bai, B. Sun and F. Gao, *Nat. Commun.*, 2021, **12**, 4831–4841.

8 J. H. Han, T. Samanta, Y. M. Park, H. J. Kim, N. S. Manikanta Viswanath, H. W. Kim, B. K. Cha, S. B. Cho and W. B. Im, *ACS Energy Lett.*, 2023, **8**, 545–552.

9 W. Pan, H. Wu, J. Luo, Z. Deng, C. Ge, C. Chen, X. Jiang, W.-J. Yin, G. Niu, L. Zhu, L. Yin, Y. Zhou, Q. Xie, X. Ke, M. Sui and J. Tang, *Nat. Photonics*, 2017, **11**, 726–732.

10 X. Ou, X. Qin, B. Huang, J. Zan, Q. Wu, Z. Hong, L. Xie, H. Bian, Z. Yi, X. Chen, Y. Wu, X. Song, J. Li, Q. Chen, H. Yang and X. Liu, *Nature*, 2021, **590**, 410–415.

11 Y. Liu, Y. Zhang, X. Zhu, J. Feng, I. Spanopoulos, W. Ke, Y. He, X. Ren, Z. Yang, F. Xiao, K. Zhao, M. Kanatzidis and S. Liu, *Adv. Mater.*, 2021, **33**, 2006010.

12 J. Casanova-Chafer, R. Garcia-Aboal, P. Atienzar and E. Llobet, *ACS Sens.*, 2022, **7**, 3753–3763.

13 A. Waleed, M. M. Tavakoli, L. Gu, Z. Wang, D. Zhang, A. Manikandan, Q. Zhang, R. Zhang, Y.-L. Chueh and Z. Fan, *Nano Lett.*, 2017, **17**, 523–530.

14 S. Tsuda and K. Saito, *J. Environ. Radioact.*, 2017, **166**, 419–426.

15 T. Igashira, N. Kawano, G. Okada, N. Kawaguchi and T. Yanagida, *Optik*, 2018, **155**, 36–42.

16 R. Hawrami, E. Ariesanti, A. Farsoni, D. Szydel and H. Sabet, *Crystals*, 2022, **12**, 1517–1525.

17 C. Kang, H. Rao, Y. Fang, J. Zeng, Z. Pan and X. Zhong, *Angew. Chem., Int. Ed.*, 2021, **60**, 660–665.

18 L. Dai, Z. Deng, F. Auras, H. Goodwin, Z. Zhang, J. C. Walmsley, P. D. Bristowe, F. Deschler and N. C. Greenham, *Nat. Photonics*, 2021, **15**, 696–702.

19 Z. Chen and T. P. Dhakal, *Appl. Phys. Rev.*, 2023, **10**, 011404.

20 G. Kresse, *J. Non-Cryst. Solids*, 1995, **192**, 222–229.

21 G. Kresse and J. Hafner, *Phys. Rev. B: Condens. Matter Mater. Phys.*, 1994, **49**, 14251–14269.

22 G. Kresse and J. Furthmüller, *Comput. Mater. Sci.*, 1996, **6**, 15–50.

23 G. Kresse and J. Furthmüller, *Phys. Rev. B: Condens. Matter Mater. Phys.*, 1996, **54**, 11169–11186.

24 G. Kresse and J. Hafner, *J. Phys.: Condens. Matter.*, 1994, **6**, 8245.

25 G. Kresse and D. Joubert, *Phys. Rev. B: Condens. Matter Mater. Phys.*, 1999, **59**, 1758–1775.

26 J. P. Perdew, K. Burke and M. Ernzerhof, *Phys. Rev. Lett.*, 1996, **77**, 3865–3868.

27 D. N. Dirin, A. Vivani, M. Zacharias, T. V. Sekh, I. Cherniukh, S. Yakunin, F. Bertolotti, M. Aebli, R. D. Schaller, A. Wieczorek, S. Siol, C. Cancellieri, L. P. H. Jeurgens, N. Masciocchi, A. Guagliardi, L. Pedesseau, J. Even, M. V. Kovalenko and M. I. Bodnarchuk, *Nano Lett.*, 2023, **23**, 1914–1923.

28 B.-Q. Zhao, Y. Li, X.-Y. Chen, Y. Han, S.-H. Wei, K. Wu and X. Zhang, *Adv. Sci.*, 2023, **10**, 2300386.

29 X. Lü, C. Stoumpos, Q. Hu, X. Ma, D. Zhang, S. Guo, J. Hoffman, K. Bu, X. Guo, Y. Wang, C. Ji, H. Chen, H. Xu,

9984 | *J. Mater. Chem. C*, 2024, **12**, 9978–9985

This journal is © The Royal Society of Chemistry 2024

Q. Jia, W. Yang, M. G. Kanatzidis and H.-K. Mao, *Natl. Sci. Rev.*, 2021, **8**, nwaa288.

30 T. Harami, S. Kakigi and A. Okuda, *J. Phys. Soc. Jpn.*, 1987, **56**, 4157–4161.

31 Y. Wang, Y. Jiao, H. Yan, G. Yang, C. Tian, A. Wu, Y. Liu and H. Fu, *Angew. Chem., Int. Ed.*, 2022, **61**, e202116233.

32 W. Xu, B. Chen, Z. Zhang, Y. Liu, Y. Xian, X. Wang, Z. Shi, H. Gu, C. Fei, N. Li, M. A. Uddin, H. Zhang, L. Dou, Y. Yan and J. Huang, *Nat. Photonics*, 2024, **18**, 379–387.

33 K. Li, Y. Shao, H. Yan, Z. Lu, K. J. Griffith, J. Yan, G. Wang, H. Fan, J. Lu, W. Huang, B. Bao, X. Liu, C. Hou, Q. Zhang, Y. Li, J. Yu and H. Wang, *Nat. Commun.*, 2018, **9**, 4798–4809.

34 F. Zhang, D. Yang, Z. Shi, C. Qin, M. Cui, Z. Ma, L. Wang, M. Wang, X. Ji, X. Chen, D. Wu, X. Li, L. Zhang and C. Shan, *Nano Today*, 2021, **38**, 101153.

35 J. Zhou, M. Li, L. Ning, R. Zhang, M. S. Molokeev, J. Zhao, S. Yang, K. Han and Z. Xia, *J. Phys. Chem. Lett.*, 2019, **10**, 1337–1341.

36 S. Tongay, J. Suh, C. Ataca, W. Fan, A. Luce, J. S. Kang, J. Liu, C. Ko, R. Raghunathanan, J. Zhou, F. Ogletree, J. Li, J. C. Grossman and J. Wu, *Sci. Rep.*, 2013, **3**, 2657–2662.

37 Y. Zhu, J. Lim, Z. Zhang, Y. Wang, S. Sarkar, H. Ramsden, Y. Li, H. Yan, D. Phuyal, N. Gauriot, A. Rao, R. L. Z. Hoye, G. Eda and M. Chhowalla, *ACS Nano*, 2023, **17**, 13545–13553.

38 Y. He, S. Liu, Z. Yao, Q. Zhao, P. Chabera, K. Zheng, B. Yang, T. Pullerits and J. Chen, *J. Phys. Chem. Lett.*, 2023, **14**, 7665–7671.

39 M. B. Bebek, C. M. Stanley, T. M. Gibbons and S. K. Estreicher, *Sci. Rep.*, 2016, **6**, 32150–32158.

40 K. Wu, A. Bera, C. Ma, Y. Du, Y. Yang, L. Li and T. Wu, *Phys. Chem. Chem. Phys.*, 2014, **16**, 22476–22481.

41 Z. Chen, C. Yu, K. Shum, J. J. Wang, W. Pfenninger, N. Vockic, J. Midgley and J. T. Kenney, *J. Lumin.*, 2012, **132**, 345–349.

42 W. Stadler, D. M. Hofmann, H. C. Alt, T. Muschik, B. K. Meyer, E. Weigel, G. Müller-Vogt, M. Salk, E. Rupp and K. W. Benz, *Phys. Rev. B: Condens. Matter Mater. Phys.*, 1995, **51**, 10619–10630.

43 C. M. Iaru, A. Brodu, N. J. J. van Hoof, S. E. T. ter Huurne, J. Buhot, F. Montanarella, S. Buhbut, P. C. M. Christianen, D. Vanmaekelbergh, C. de Mello Donega, J. G. Rivas, P. M. Koenraad and A. Y. Silov, *Nat. Commun.*, 2021, **12**, 5844–5852.

44 M. B. de la Mora, O. Amelines-Sarria, B. M. Monroy, C. D. Hernández-Pérez and J. E. Lugo, *Sol. Energy Mater. Sol. Cells*, 2017, **165**, 59–71.

45 A. Morteza Najarian, F. Dinic, H. Chen, R. Sabatini, C. Zheng, A. Lough, T. Maris, M. I. Saidaminov, F. P. García de Arquer, O. Voznyy, S. Hoogland and E. H. Sargent, *Nature*, 2023, **620**, 328–335.

This journal is © The Royal Society of Chemistry 2024

J. Mater. Chem. C, 2024, **12**, 9978–9985 | **9985**